Bi/BSO Heterojunctions via Vacancy Engineering for Efficient Photocatalytic Nitrogen Fixation

Runjie Wu, Shuai Gao, Colton Jones, Mingming Sun, Ming Guo, Ran Tai, Shaowei Chen,* and Qiang Wang*

Photocatalytic nitrogen reduction represents a viable technology for green ammonia synthesis under mild conditions. However, the performance of the photocatalysts is typically limited by high charge carrier recombination and low adsorption and activation of nitrogen molecules. Herein, $Bi/Bi_2Sn_2O_7$ (Bi/BSO) heterojunction nanocomposites are prepared via a one-step hydrothermal method, where NaOH etching of oxygen vacancies in the Bi—O bonds of $Bi_2Sn_2O_7$ (BSO) is exploited for the in situ formation of metallic Bi and hence Schottky junctions with the semiconducting BSO. This leads to a high separation rate of photogenerated charge carriers. Consequently, compared to the pure-phase BSO, the Bi/BSO heterostructures exhibit markedly enhanced ammonia production, reaching an optimum rate of 284.5 μmol g^{-1} h^{-1}, where the rectifying contact between the semiconducting BSO and metallic Bi facilitates directional BSO to Bi electron transfer, leading to enrichment of photogenerated electrons at the active sites of metallic Bi. First-principles calculations confirm the alteration of active sites and the guided electron flow by the Schottky junctions and surface oxygen vacancies. Results from this study offer an effective paradigm of structural engineering in manipulating the photocatalytic activity of bismuth-based pyrochlore materials toward nitrogen fixation to ammonia.

1. Introduction

Ammonia is an important commodity chemical used in diverse areas.[1] Currently, ammonia is produced primarily by the energy-intensive Haber-Bosch method,[2] which is limited by the remarkable stability of N_2 molecules (with a N≡N bond energy of 941.3 kJ mol^{-1}),[3] high ionization potential (15.85 eV), and low electron affinity (−1.90 eV), resulting in substantial greenhouse gas emissions and detrimental environmental consequences.[4] Thus, extensive efforts have been devoted to the development of green technologies for artificial ammonia synthesis.[5–7] Among these, photocatalysis has emerged as a viable option owing to its mild reaction conditions and environmentally sustainable procedures. Toward this end, development of effective photocatalysts represent a critical first step.[8–10] Thus far, a range of strategies have been reported to engineer the structure and improve the performance of photocatalysts, such as defect engineering,[11–12] crystal facet regulation,[13] heteroatom doping,[14–16] and formation of metal-semiconductor heterojunctions.[17–19] Of these, metal-semiconductor heterojunctions have been found to produce a Schottky rectifying contact that can facilitate the formation of a depletion region on the semiconductor surface and a potential barrier to hinder electron transfer from the metal to the semiconductor.[20] In addition, the incorporation of metals may significantly augment photo absorption of the photocatalysts, particularly in the visible and infrared regions, due to the surface plasmon resonance (SPR) effect.[21] Both characteristics are conducive to the efficient separation of photogenerated charge carriers for maximal photocatalytic performance.

Bismuth-based pyrochlore materials have emerged as unique photocatalysts for energy storage and environmental remediation.[22–24] Of these, $Bi_2Sn_2O_7$ (BSO) features two interpenetrating metals arranged in a tetrahedral and octahedral coordination, which facilitate the separation of photogenerated charges; and the photocatalytic performance can be further enhanced by defect engineering. According to the σ donation-π* back-donation mechanism, nitrogen is adsorbed onto the active sites, and the N≡N bond is activated due to transfer of photogenerated electrons into the π* antibonding orbitals, which initializes the nitrogen reduction reaction (NRR). The efficacy of this process can be boosted by the formation of surface oxygen defects.[25–26] For instance, Di et al.[27] introduced surface oxygen vacancies by tuning the size of BSO, thereby enhancing the chemical adsorption of N_2 molecules and reducing the energy barrier for the rate-limiting step of nitrogen fixation.

R. Wu, S. Gao, M. Sun, M. Guo, R. Tai, Q. Wang
Laboratory for Micro-sized Functional Materials & College of Elementary Education and Department of Chemistry
Capital Normal University
Beijing 100048, China
E-mail: qiangwang@cnu.edu.cn
C. Jones, S. Chen
Department of Chemistry and Biochemistry
University of California
1156 High Street, Santa Cruz, CA 95064, USA
E-mail: shaowei@ucsc.edu

**ADVANCED
SCIENCE NEWS**

www.advancedsciencenews.com

**ADVANCED
FUNCTIONAL
MATERIALS**

www.afm-journal.de
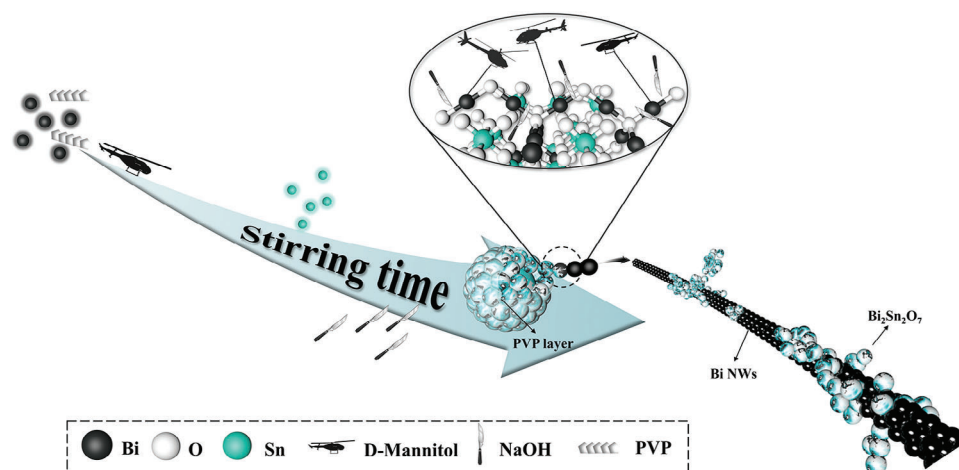
Scheme 1. Schematic of the synthesis process of Bi/BSO composites.

Furthermore, metallic Bi exhibits a high intrinsic activity in activating N_2 molecules and concurrently is mostly inert toward the competitive hydrogen evolution reaction (HER), as computational studies based on density functional theory (DFT) calculations show that the hydrogen adsorption energy (ΔG_H^*) on Bi is rather high at ca. 0.75 eV.[28–30] This suggests that the formation of Bi/BSO heterojunctions may be exploited for selective ammonia synthesis, with minimal interference from HER.[31]

In this study, Bi/BSO nanocomposites rich in oxygen vacancies were prepared via a facile hydrothermal method, which exhibited a nitrogen fixation rate as high as 284.5 μmol g^{-1} h^{-1} in pure water under simulated sunlight irradiation, with excellent stability. Such a performance was markedly better than that of pure-phase BSO. This was ascribed to the formation of oxygen vacancies and Schottky junctions that promoted charge separation, as manifested in experimental measurements and DFT calculations. Bader charge analysis showed that the metallic Bi deposited on the composite surface functioned as an electron sink, accepting multiple electrons from the semiconducting BSO, and as the active site of NRR. In situ infrared spectroscopy measurements confirmed that NH_4^+ was indeed produced from NRR, and the Gibbs free energy of the hydrogenation path and protonation energy barrier of the distal association were assessed by DFT calculations.

2. Results and Discussion

2.1. Samples Synthesis and Structural Characterization

The samples were synthesized via a one-step hydrothermal method (**Scheme 1**). Specifically, pure-phase BSO nanoparticles were prepared by hydrothermal treatment at 160 °C for 12 h of a mixture of bismuth nitrate pentahydrate (Bi(NO$_3$)$_3$ 5H$_2$O, 0.5 mmol), sodium stannate (Na$_2$SnO$_3$, 0.5 mmol), polyvinylpyrrolidone (PVP, 0.2 g), and D-mannitol (15 mL, 0.1 м), along with sodium hydroxide (NaOH, 5 mL, 0.5 м). Bi/BSO nanocomposites were obtained in the same fashion except that the concentration of NaOH was increased to 0.8, 0.9, 1.0, and 1.1 м, and referred to as Bi/BSO-X (X = 1, 2, 3, and 4), respec-

tively (Scheme 1). The experimental details are included in the Supporting Information.

The sample morphologies were first examined by scanning electron microscopy (SEM) and transmission electron microscopy (TEM) measurements. From the TEM images in Figure S1a–d (Supporting Information), it can be observed that BSO consisted of agglomerates of nanoparticles, whereas the Bi/BSO-3 composite contained nanoparticles dispersed around nanowires (that is also clearly manifested in SEM measurements, Figure S1e, Supporting Information). In high-resolution TEM (HRTEM) measurements (**Figure 1a**), the nanoparticles can be seen to exhibit well-defined lattice fringes, where the interplanar spacings of 0.215 and 0.305 nm are consistent with the orthogonal ($\bar{2}24$) and ($2\bar{2}2$) crystal planes of BSO, respectively. This is also manifested in the Fast Fourier Transform (FFT) and Inverse Fast Fourier Transform (IFFT) patterns in Figure 1b. The results indicate that the material conforms to the ICSD#50 311 lattice parameters (a = b = c = 10.7225 Å, α = β = γ = 90°) and grows along the [110] crystal orientation. Such a crystal structure consists of a 3D network with alternating arrangements of the Bi and Sn atoms, and oxygen atoms filling the gaps in the 3D network, with two coordination environments, O^1 (Bi-O) and O^2 (Sn-O) (Figure S2, Supporting Information). For the nanowire in Bi/BSO (Figure 1c; Figure S3, Supporting Information), the diffraction spots of the ($01\bar{2}$), ($\bar{1}0\bar{2}$), and ($\bar{1}\bar{1}0$) crystal planes of metallic Bi can be readily resolved. In fact, the crystal structure can be found to be consistent with ICSD#246 663, where the interplanar spacings of 0.31 and 0.216 nm correspond to the (012) and ($\bar{1}\bar{1}0$) planes of metallic Bi, respectively, with a crystal plane angle of 44°, and growth along the [$2\bar{2}1$] crystal phase. Again, the crystal plane exposures and growth axes can also be evidenced in the FFT and IFFT patterns of the HRTEM images of BSO nanoparticle and Bi nanowire (Figure 1d; Figure S3, Supporting Information), which are in excellent agreement with the crystal structures of BSO along [110] and Bi along [$2\bar{2}1$] (Figure 1e,f). Consistent results were obtained in elemental mapping analysis based on energy-dispersive X-ray spectroscopy (EDS) (Figure 1g), where the elements of Bi, Sn, and O can be found to be distributed rather evenly across the sample with the nanowires enriched with Bi. Taken together, these results indicate the formation of a
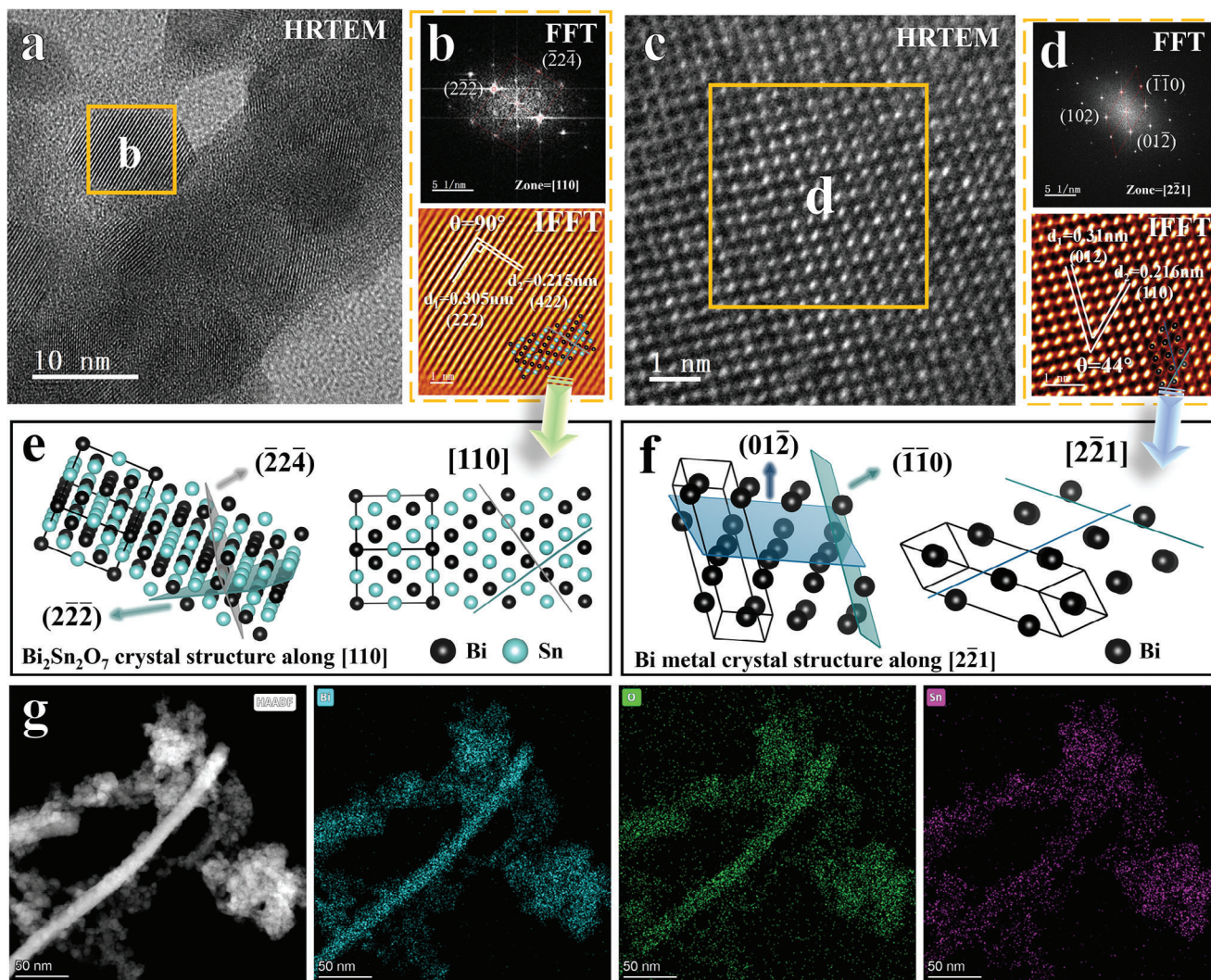
**ADVANCED
SCIENCE NEWS**

www.advancedsciencenews.com

**ADVANCED
FUNCTIONAL
MATERIALS**

www.afm-journal.de

Figure 1. a,c) HRTEM image and b,d) the corresponding FFT and IFFT patterns of (a,b) BSO nanoparticles and (c,d) Bi nanowires of Bi/BSO composites. e,f) Crystal structure diagrams of (e) pyrochlore BSO and (f) metal Bi. g) EDS-based elemental mapping analysis of Bi/BSO-3.

heterojunction interface between Bi and BSO in the Bi/BSO samples (Figure S4, Supporting Information).

For control samples prepared without PVP (Bi-3) or D-mannitol (BSO-3) (Figure S5, Supporting Information), it was observed that the BSO substrate in Bi-3 was damaged, while no elemental Bi was produced in BSO-3. This suggests that PVP played a major role in the protection of the BSO structure and the formation of well-crystallized Bi nanowires,[32] whereas D-Mannitol was a crucial reducing agent for the hydrothermal production of metallic Bi. In the preparation of the Bi/BSO samples, the etching effect of NaOH was utilized to control the amount of Bi produced due to manipulation of the D-Mannitol reactivity,[33–35] which was critical in the formation of metallic Bi active sites for nitrogen fixation (vide infra).

In powder X-ray diffraction (PXRD) measurements (**Figure 2a**), the BSO and Bi/BSO samples can all be seen to exhibit a series of diffraction peaks at $2\theta = 28.76°$, $33.33°$, $47.86°$ and $56.80°$ that may be assigned to the (222), (400), (440), and (622) crystalline planes of BSO (ICSD#50 311), respectively.

For the Bi/BSO samples, three additional peaks appeared at $2\theta = 27.16°$, $37.95°$ and $39.61°$, due respectively to the (012), (104), and (110) crystal planes of metallic Bi (ICSD#246 663), and the peak intensity increased with an increase of the NaOH feed in sample synthesis; concurrently, the diffraction peaks of $Bi_2Sn_2O_7$ became weakened. These observations are consistent with the NaOH-enhanced production of metallic Bi, leading to the formation of Bi/BSO heterojunctions, as observed in the above TEM and SEM measurements.

The elemental composition and valency were then analyzed by X-ray photoelectron spectroscopy (XPS) measurements. From the survey spectra in Figure 2b, the Bi, Sn, and O elements can all be readily resolved in both Bi/BSO-3 and BSO. The high-resolution Bi 4f scans are shown in Figure 2c. BSO can be seen to possess a doublet at 158.81 and 164.14 eV, due to the $4f_{7/2}$ and $4f_{5/2}$ electrons of Bi^{3+}; by contrast, two doublets can be resolved in Bi/BSO-3, where the Bi^{3+} doublet appeared at 158.67 and 163.99 eV, and the other doublet at 157.0 and 162.3 eV is consistent with the $4f_{7/2}$ and $4f_{5/2}$ electrons of metallic Bi.[20] This
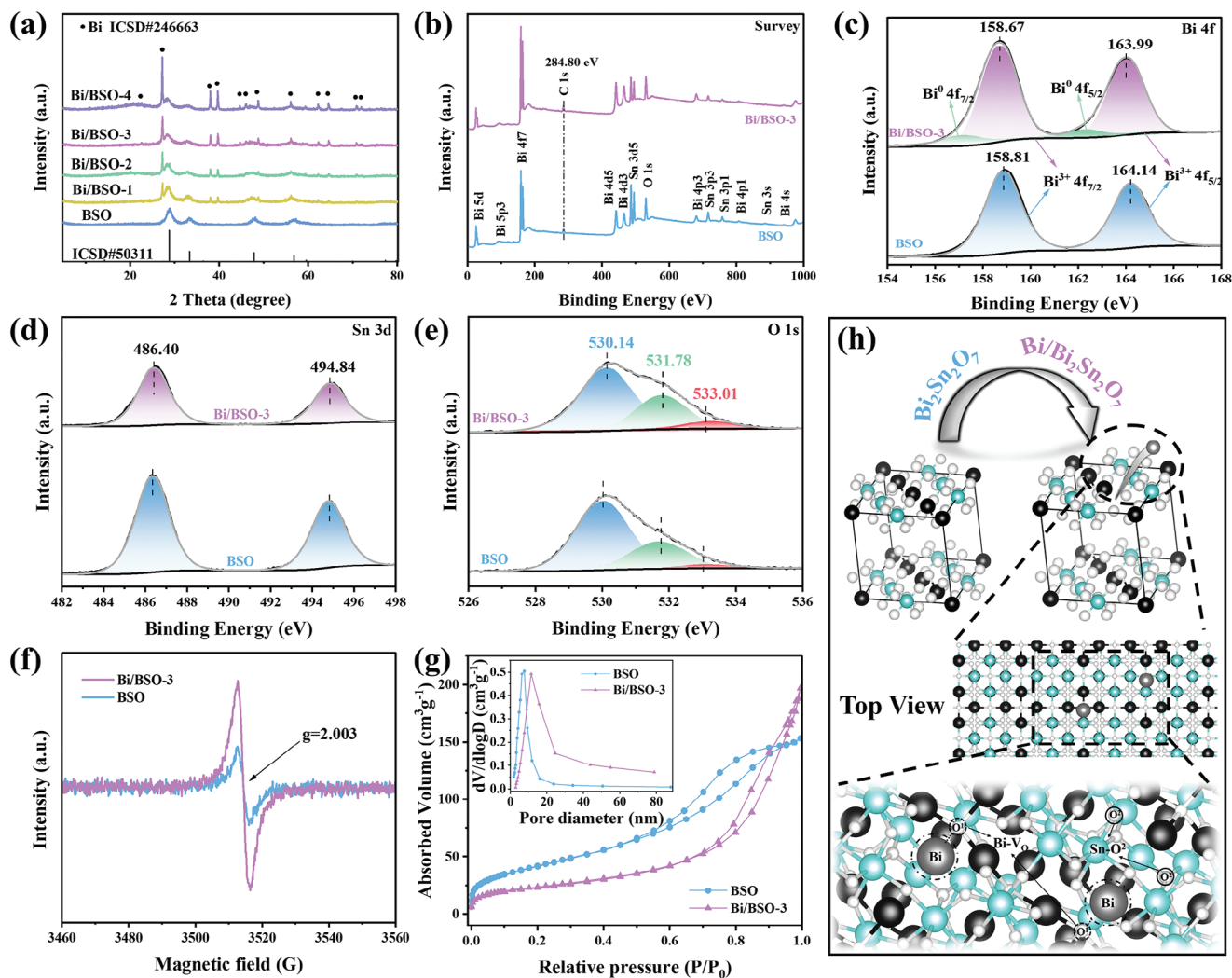
ADVANCED
SCIENCE NEWS

www.advancedsciencenews.com

ADVANCED
FUNCTIONAL
MATERIALS

www.afm-journal.de

Figure 2. a) XRD patterns of BSO and Bi/BSO-X (X = 1, 2, 3, and 4). b) XPS survey spectra, and high-resolution scans of the c) Bi 4f, d) Sn 3d, and e) O 1s electrons of BSO and Bi/BSO-3. f) EPR spectra of BSO and Bi/BSO-3. g) N_2 adsorption isotherms of BSO and Bi/BSO-3. Inset is the pore size distribution. h) Atomic structure of BSO and the production of metallic Bi, along with the top-view diagram of the position for the generation of oxygen vacancy.

is, again, in good agreement with the formation of Bi/BSO heterojunctions in Bi/BSO-3. Notably, the Bi^{3+} binding energies of BSO and Bi/BSO-3 were all somewhat lower than the standard values (159.07 and 164.38 eV), suggesting a reduced valency of the Bi species likely due to oxygen vacancies. And the fact that the binding energies of Bi/BSO were slightly lower than those of BSO can be ascribed to a higher vacancy concentration in the former, consistent with results from further measurements (e.g., Figure 2f). Figure 2d shows the Sn 3d spectra, where the binding energies of the $3d_{5/2}$ and $3d_{3/2}$ doublet remained almost identical for the two samples at 486.40 and 494.84 eV for Sn^{4+}, indicating a consistent surface coordination environment of the Sn centers.[20,36,37] Deconvolution of the O 1s spectra (Figure 2e) yielded three peaks, lattice oxygen ($O_{lat.}$, 530.1 eV), surface defect oxygen ($O_{def.}$, 531.7 eV), and oxygen-containing species adsorbed on the sample surface ($O_{ads.}$, 533.0 eV, that were most likely surface OH species, vide infra).[38] Notably, both O_{def} and O_{ads} peaks of Bi/BSO-3 became apparently intensified, in com-

parison to those of BSO, suggesting an increase of oxygen vacancies and enhanced production of surface hydroxyl species.

Consistent results were obtained in electron paramagnetic resonance (EPR) measurements (Figure 2f), where the oxygen vacancy signals (g = 2.003) were markedly stronger with Bi/BSO-3 than with BSO. Taken together, these results suggest that oxygen vacancies most likely occurred at the O^1 (Bi—O) position, where the Bi—O bonds were ruptured by NaOH etching, rendering the oxygen atoms to transfer electrons to the bonding Bi atoms, thus leading to the deposition of metallic Bi on the sample surface.

Brunauer-Emmett-Teller (BET) measurements were then performed to determine the specific surface area and porosity of the samples. From Figure 2g, both BSO and Bi/BSO can be seen to exhibit a type IV isotherm, suggesting the formation of mostly mesopores, with a respective specific surface area of 154.0 and 85.1 m^2 g^{-1}. The decrease in the specific surface area of Bi/BSO can be attributed to the transformation of some 0D nanoparticles into 1D nanowires. Notably, the average pore size
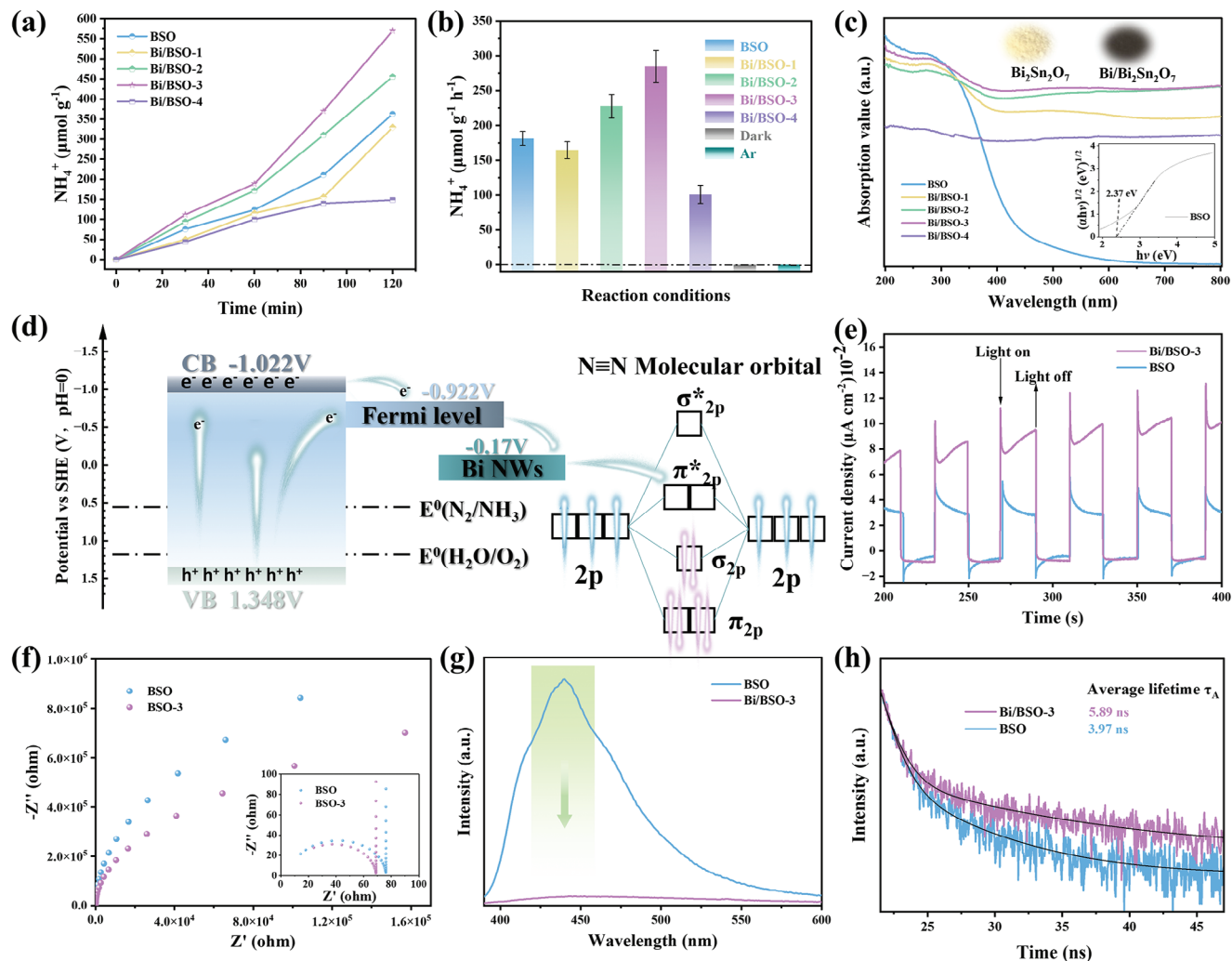
ADVANCED
SCIENCE NEWS

www.advancedsciencenews.com

ADVANCED
FUNCTIONAL
MATERIALS

www.afm-journal.de

Figure 3. a) Time-dependent photocatalytic ammonia production by BSO and Bi/BSO-X. b) Photocatalytic NH_4^+ production rates of various samples and in other environments (dark and Ar purging). c) UV–vis absorption reflectance spectra of BSO and Bi/BSO-3. Top inset is the photographs of BSO and Bi/BSO, and bottom Inset is the Tauc plot of BSO. d) Schematic diagram of band structure of nitrogen reduction and electron transition of nitrogen molecular orbitals. e) Photocurrent responses of periodic light switching, f) Nyquist plots (inset is the zoom in of the low impedance region), g) steady-state and h) time-resolved photoluminescence spectra of BSO and Bi/BSO-3.

of Bi/BSO (12.96 nm) was significantly larger than that of BSO (5.76 nm) (Figure 2g inset), likely due to the generation of oxygen vacancies and the precipitation of Bi atoms into metallic nanowires, leading to an increase of surface defects in the sample (Figure 2h).

2.2. Photocatalytic Activity

The photocatalytic activity of the samples toward nitrogen fixation for ammonia synthesis was then evaluated under simulated sunlight in pure water. The NH_4^+ yields of all samples were quantitatively assessed in triplicates using the Nessler reagent colorimetric method,[39] with the calibration curve depicted in Figure S6 (Supporting Information). From **Figure 3a**, it can be seen that Bi/BSO-3 exhibited the best performance among the Bi/BSO composites and was almost 50% better than BSO, reaching a pro-

duction rate of 284.5 µmol g^{-1} h^{-1}. Notably, during the nitrogen fixation process, only a small amount of oxygen was produced (Figure S7, Supporting Information), and no hydrogen was observed, due to effective inhibition of hydrogen evolution by the formation of elemental Bi.[28–30] Yet the fact that the photocatalytic activity diminished markedly with an excess of Bi can be ascribed to weakened synergy at the Bi-Bi$_2$Sn$_2$O$_7$ interface by excessive NaOH etching where Bi was formed at the expense of the Bi$_2$Sn$_2$O$_7$ scaffold. Furthermore, no NH_4^+ was detected in the dark or in an argon atmosphere, indicating that the ammonia detected indeed originated from the photocatalytic reduction of N$_2$. Bi/BSO-3 also exhibited remarkable stability. After four cycles of nitrogen fixation experiments, about 80% of the ammonia production rate was retained at 224.6 µmol g^{-1} h^{-1} (Figure S8, Supporting Information). Additionally, there were no significant changes in sample morphology and structure, except for only a slight decrease of oxygen vacancy concentration, which coincided

with the small diminishment of the photocatalytic performance (Figures S9–S11, Supporting Information).

To unravel the mechanistic insights of metallic Bi in the photocatalytic NRR process, a series of characterizations were performed to examine the optoelectronic properties of the samples. The BSO sample exhibited a yellow color appearance, whereas Bi/BSO showed a black color due to the formation of metallic Bi nanoparticles, which is anticipated to enhance photo absorption in the visible range. Indeed, in ultraviolet-visible diffuse reflectance spectroscopy (UV–vis DRS) measurements (Figure 3c), BSO exhibited an absorption threshold of ca. 425 nm, whereas the absorption of Bi/BSO composites was extended to the visible region. It is noteworthy that a weak broad peak appeared at ≈500 nm with the Bi/BSO composites, most likely due to the SPR of metallic Bi nanoparticles.[40–42] In addition, from the corresponding Tauc plots (Figure 3c inset), the bandgap was estimated to be 2.37 eV for BSO, which is somewhat lower than that of pristine BSO (2.6 eV),[43] likely due to the formation of surface oxygen vacancies. From the Mott–Schottky plots of BSO at different frequencies (Figure S12, Supporting Information), the flat potential was estimated to be −0.922 V versus SHE (standard hydrogen electrode) and the carrier concentrations at different frequencies are shown in Figure S13 (Supporting Information). The positive slope indicates that BSO is an n-type semiconductor, with a flat potential close to the conduction band. The potentials of the conduction band (E_{CB}) and valence band (E_{VB}) were then estimated to be −1.022 and 1.348 V versus SHE, respectively. From the Urbach tail of the BSO sample which arose from oxygen vacancies, the Urbach energy (E_u) was calculated to be 0.41 eV. Note that Urbach energy is correlated to the defect concentration of the crystal, and is typically manifested with an additional absorption band, leading to enhanced photo absorption.[44]

The band structure of the Bi/BSO composites is shown in Figure 3d, along with the molecular orbital diagram of nitrogen gas, where photogenerated electrons are transferred to Bi, and eventually to the π^* antibonding orbitals of adsorbed N_2, breaking the N—N triple bond for nitrogen reduction.

We then performed photoelectrochemical measurements to analyze the separation, transfer, and recombination of photogenerated charge carriers of the samples under simulated sunlight irradiation. It can be seen from Figures 3e and S14 (Supporting Information) that the Bi/BSO composites exhibited a significantly higher transient photocurrent response (TRCP) than BSO, indicating that the charge layers on the surfaces of the metal and semiconductor resulted in a potential difference, accelerating the electron transfer to the surface and hence enhancing the surface electron density.[45] In electrochemical impedance spectroscopy (EIS) measurements (Figure 3f), Bi/BSO-3 displayed a smaller arc diameter of the Nyquist plot (charge transfer resistance, R_{CT}) than BSO, which is favorable for carrier transport and separation. It is worth noting that although Bi/BSO-4 showed excellent performance in TRCP and EIS measurements (Figures S14 and S15, Supporting Information), its ammonia synthesis performance was low, likely because excessive metallic Bi nanoparticles led to the loss of active sites, making the adsorption and activation of N_2 difficult.

Consistent results were obtained in steady-state photoluminescence (PL) measurements. One can see that at the excitation wavelength (λ_{ex}) of 370 nm (Figure 3g), the emission peak

red-shifted to 450 nm for Bi/BSO-3 from 440 nm for BSO, due to the change of the energy band structure. Meanwhile, the PL emission of Bi/BSO-3 was drastically quenched as compared to that of BSO, suggesting markedly impeded recombination of the photogenerated carriers in the former. That is, the formation of Bi/BSO heterojunctions significantly improved the charge separation efficiency. Indeed, in time-resolved photoluminescence (TRPL) measurements (Figure 3h; Table S1, Supporting Information), it can be seen that whereas the decay lifetime (τ_1) of trapped states by surface defects is similar (1.02 vs 1.05 ns), the decay lifetime (τ_2) of direct transition radiation increased from 6.41 ns in BSO to 9.28 ns in Bi/BSO-3, which can be attributed to the Schottky barrier that prevented electrons from flowing back from metal to semiconductor to recombine with holes. The corresponding average PL lifetime ($\tau_{avg} = \frac{A_1\tau_1^2 + A_2\tau_2^2}{A_1\tau_1 + A_2\tau_2}$, Table S1, Supporting Information) was also found to increase from 3.97 nm for BSO to 5.89 ns for Bi/BSO-3, consistent with enhanced separation of photogenerated charges in the latter.

The work function of Bi is 4.36 eV (vs vacuum),[46] and the Fermi level of metallic Bi (E_{Fm}) is −0.17 V (vs SHE), lower than the Fermi level of BSO. When metallic Bi and semiconducting BSO came into contact forming a heterojunction, electrons in the semiconductor would flow to the lower level on the metal side, creating a positive space charge region on the semiconductor surface, causing the semiconductor band to bend upward and form a barrier layer that allowed only unidirectional electron flow from the semiconductor to the metal. This produced a rectifying Schottky barrier diode (SBD), with the corresponding potential barrier known as the Schottky barrier, which enhanced the separation of photogenerated charges.[47] Figure S16 (Supporting Information) shows the SBD energy band diagram of Bi/BSO. If the surface effect of the semiconductor is ignored, the metal and the semiconductor have the same Fermi level in the equilibrium state after they are in close contact. For the same kind of semiconductor, the electron affinity remains constant at all times, so the Schottky barrier changes with the work function of the metal, and the height of the Schottky barrier on the metal side can be calculated to be 0.852 eV for Bi/BSO. However, the measured value often has nothing to do with the work function of metal. Usually, the empirical value of the Schottky barrier height of n-type semiconductor is $2E_g/3$. This is because the surface state leads to the formation of an energy level $q\varphi_0$ on the semiconductor surface, which is ≈1/3 of the forbidden bandwidth. The energy band bends before contacting the metal, and the Fermi levels of the semiconductor and the metal are pinned at $E_g/3$ after contacting. In addition to the intrinsic surface state caused by dangling bonds due to the surface lattice interruption, the n-type semiconductor BSO also contained extrinsic surface states caused by defects, and it is difficult to ignore the influence of surface effect. Therefore, we also included the energy band model of the new SBD (**Figure 4**), and recalculated the barrier height on the metal side as 1.58 eV.

To confirm the source of ammonia, in situ Fourier-transform infrared (FTIR) tests were performed on Bi/BSO-3.[48,49] **Figure 5a** displays the FTIR spectra obtained under a continuous nitrogen gas flow in the dark, where a series of vibrational bands can be resolved, peak I (1668 cm^{-1}), peak II (1713 cm^{-1}), peak III (3050 cm^{-1}), peak IV (3380 cm^{-1}), and peak V (3610 cm^{-1}), due to chemisorbed N_2, NH_3, NH_4^+, hydroxyl
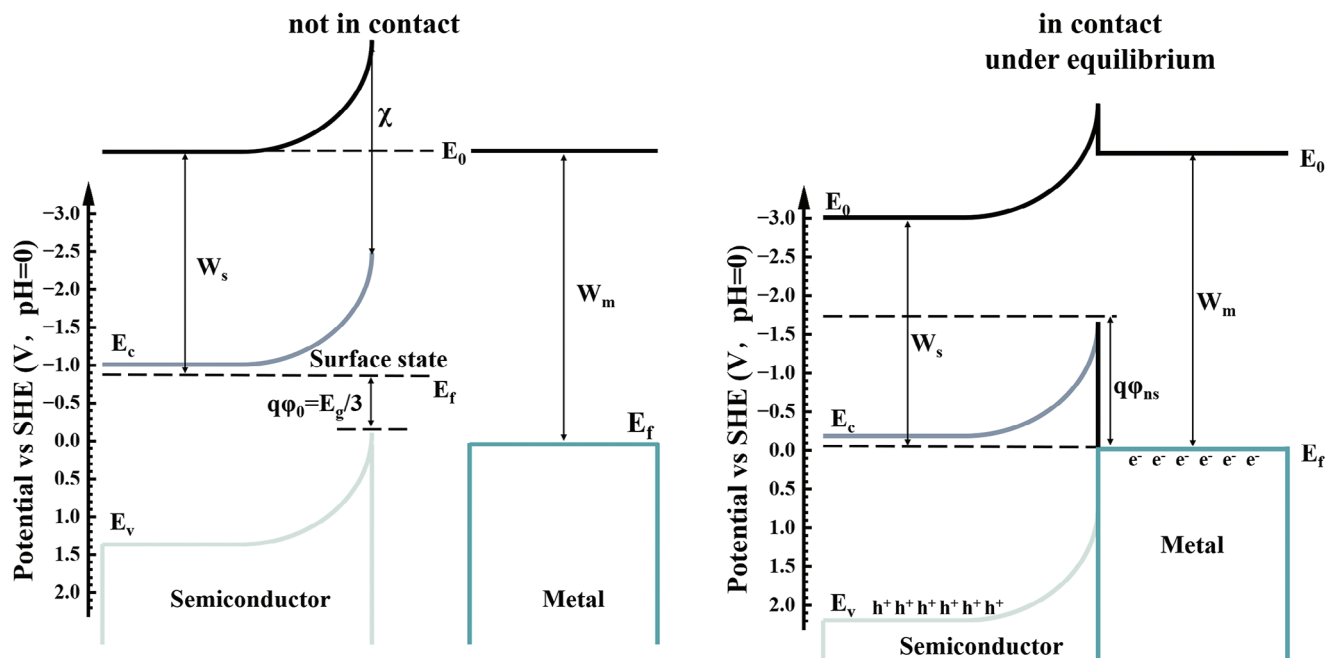
Figure 4. Energy band diagram of *n*-type semiconductor BSO with high surface state before and after contact with metal Bi. (χ, electron affinity energy; $q\varphi_0$, distance between surface energy level and valence band top; W_s, work function of semiconductor; W_m, work function of metal).

groups, and N—H bonds, respectively.[15,27,50–52] Yet, under simulated sunlight irradiation (Figure 5b,c), the FTIR profiles exhibited a dynamic variation, likely because photogenerated charges initiated the adsorption and protonation reactions of N_2 on the catalyst surface. For instance, peaks i (1070 cm^{-1}), ii (1308 cm^{-1}), and iv (1600 cm^{-1}) in Figure 5b can be attributed to the N—N stretching vibration, NH_3 adsorption, and chemical adsorption of N_2, respectively; and peaks iii (1416 cm^{-1}) and vi (2880 cm^{-1}) are due to the characteristic vibrations of NH_4^+.

These results indicate that N_2 was successfully converted to NH_3 and NH_4^+ after being adsorbed onto the catalyst surface. Indeed, peaks v (1650 cm^{-1}) and viii (3390 cm^{-1}) in Figure 5c can be assigned to the N—H bending and stretching vibrations; and peaks vii (3230 cm^{-1}) and ix (3748 cm^{-1}) are attributed to O—H stretching vibrations.[53,54] Note that no characteristic peaks of N_2H_4 (1129 and 1290 cm^{-1}) were detected (Figure S17, Supporting Information). As the protonation of N_2 can be facilitated by surface OH species, these results show that photocatalytic
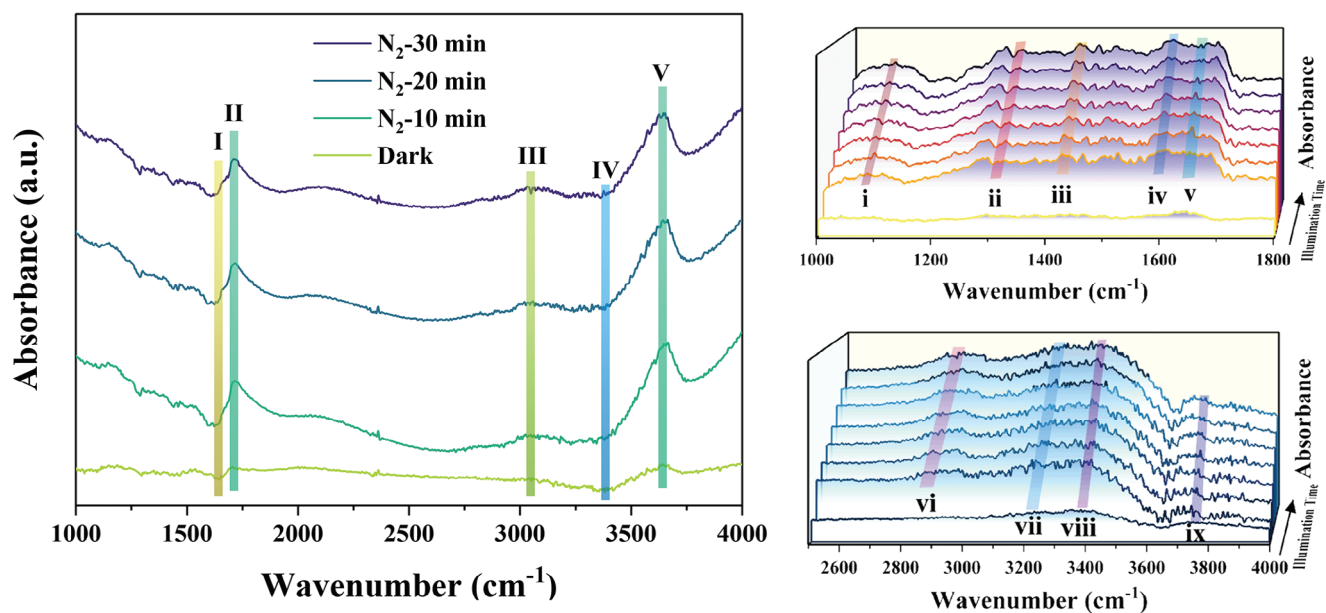

Figure 5. In situ FTIR spectra of Bi/BSO-3 a) in the dark and b,c) under photoirradiation for up to 70 min.

**ADVANCED
SCIENCE NEWS**

www.advancedsciencenews.com

**ADVANCED
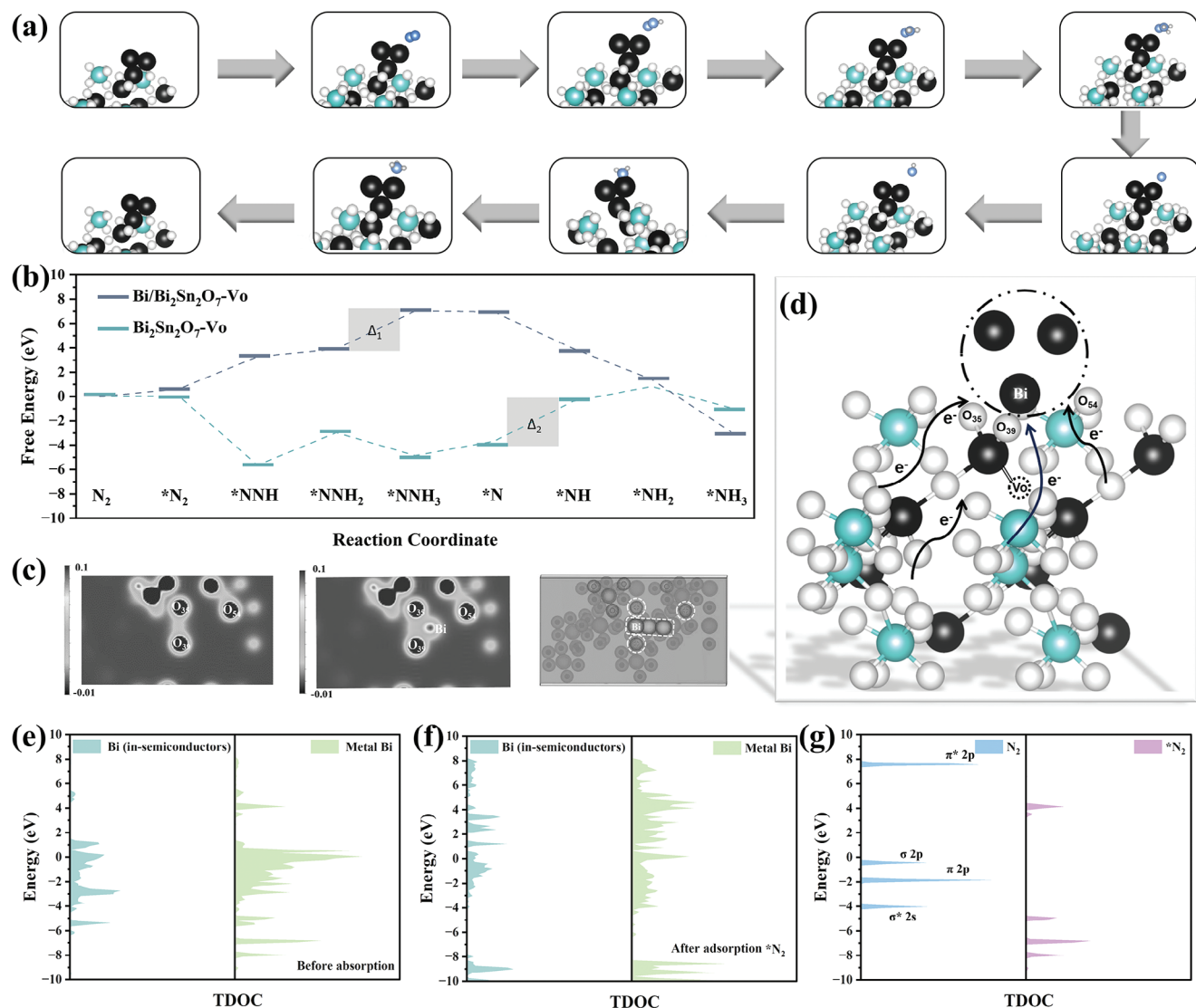FUNCTIONAL
MATERIALS**

www.afm-journal.de

Figure 6. a) Schematic diagram of the NRR pathway on Bi/BSO-Vo. b) Reaction energy diagram of nitrogen fixation photocatalyzed by BSO-Vo and Bi/BSO-Vo. c) Electron density (ED) of Bi/BSO-Vo. d) Schematic diagram of charge transfer pathways based on Bader charge analysis. e–g) TDOS in and out of Bi/BSO-Vo models before and after activation of N_2 molecules.

nitrogen reduction on Bi/BSO-3 followed the distal coupling pathway, where the synergistic effect of surface hydroxylation and photogenerated electrons facilitated N_2 adsorption, activation of inert N≡N bonds, and N—N cracking.[15] And the fact that Bi/BSO-3 clearly outperformed BSO in photocatalytic NRR (Figure 3a,b) is consistent with results from XPS measurements that showed an apparent increase of the O_{ads} species (Figure 2e).

In addition, we carried out isotope labeling experiments in a closed reaction system. As shown in Figure S18 (Supporting Information), we first made a standard sample of $^{14}NH_4Cl$. When $^{15}N_2$ is used as the feed gas, it can be clearly observed that there are two symmetrical splitting cracks in ^1H nuclear magnetic resonance (NMR) measurements, which are attributed to the coupling of ^1H and ^{15}N. The results further confirmed that ammonia was produced from the feed nitrogen gas rather than other nitrogen-containing impurities.[55]

2.3. Theoretical Study

DFT calculations were then carried out to study the synergistic interaction between the Bi nanoparticles and oxygen vacancies and their influence on the nitrogen fixation mechanism. Two BSO models were constructed based on the above experimental results, one containing only oxygen vacancies (BSO-Vo) and the other with both Bi deposition and oxygen vacancies (Bi/BSO-Vo). Initially, N_2 chemisorbs at the active site and transforms into *NN (* denotes surface-adsorbed species) in both models. **Figure 6a** illustrates the atomic model of the hydrogenation step on the Bi/BSO-Vo surface, where N_2 preferentially adsorbs on the exposed facets and binds to the metallic Bi, following a terminal binding mechanism. The Gibbs free energy profiles of NRR on BSO-Vo and Bi/BSO-Vo were then constructed and shown in Figure 6b, which can be seen to exhibit a contrasting trend,

with the respective rate-determining steps being $*N + H^+ \rightarrow *NH$ (Δ2) and $*NNH_2 + H^+ \rightarrow *NNH_3$ (Δ1). Additionally, BSO-Vo displays a somewhat higher energy barrier of 3.3 eV for the hydrogenation step (Δ2), in comparison to 3.1 eV for Bi/BSO-Vo in (Δ1). Furthermore, the comprehensive pathway of ammonia synthesis on Bi/BSO-Vo is exothermic, releasing an energy of −2.88 eV, thus displaying enhanced energy selectivity. Importantly, the final hydrogenation step ($*NNH_3 \rightarrow *NH_3$) is energetically viable.

N_2 adsorbs onto nearby Bi atoms at symmetric sites in the BSO-Vo model, and during the protonation process, an alternating hydrogenation pattern involving asymmetric and symmetric sites emerges. However, due to the inherent Schottky barrier at the Bi/BSO interface, electrons are accumulated on metallic Bi, inducing alterations in the active sites. This was indeed confirmed in temperature-programmed desorption (TPD) measurements of N_2 (Figure S19, Supporting Information). BSO exhibited characteristic peaks similar to those reported previously,[27] whereas the desorption peaks of Bi/BSO showed pronounced changes.

From the electron density (ED) plots in Figure 6c, one can see that photogenerated charges initially accumulate at the surface O atoms of the crystal and progressively shift toward metallic Bi, effectively simulating the Schottky barrier effect. To elucidate the electron flow pathway and highlight the extent of charge transfer more clearly, Bader charge analysis was conducted which reveals 45 additional electrons in Bi/BSO-Vo as compared to the original structure (Table S2, Supporting Information). The charge migrates through other nearby O atoms (O_{35}, O_{39}, O_{54}) around the oxygen vacancies, ultimately transferring to the Bi metal (Figure 6d). The charge accumulation, in conjunction with the Schottky junction effect and oxygen vacancies, collectively dictates the electron flow and facilitates the activation of N_2 molecules, endowing Bi/BSO-Vo with an outstanding nitrogen fixation activity (Figure S20, Supporting Information).

Furthermore, to elucidate the electronic structure and bonding properties of the catalytic system during the hydrogenation of N_2 molecules, the Bi/BSO-Vo model was divided into internal semiconductor Bi atoms and externally loaded metallic Bi. The density of states (DOS) before and after N_2 adsorption and activation on the Bi/BSO-Vo surface was assessed. From Figure 6e one can see that before N_2 adsorption, the surface Bi (Metal Bi) possesses a larger number of electrons and higher energy compared to the internal Bi, promoting subsequent electron transfer and bonding. Upon N_2 adsorption, an evident arrangement of the energy level favorable for π* orbital interactions in the post-adsorption DOS is observed, indicating a more dynamic local electronic structure that enhances N_2 activation (Figure 6f). Electron injection causes the electronic states of N to shift toward lower energy regions and initiate splitting (Figure 6g). The more interaction with the π* orbitals, the greater the occupancy, leading to a lower NN bond order.[56] The energy matching is poor between the Bi metal and the σ* 2s antibonding orbitals and σ 2p, π 2p bonding orbitals below the Fermi level. Meanwhile, the overlap between the Bi 6p and N π* 2p antibonding orbitals leads to partial occupation of the formed p-π* orbitals. Electron transfer from the metal to $*N_2$ thereby weakens the NN bond. In the subsequent protonation process, metallic Bi still maintains a favorable energy level (Figure S21, Supporting Information), and some electronic states

of the metallic Bi also experience slight reduction, indicating the effective utilization of photogenerated electrons in the process of breaking the N≡N bonds. In short, metallic Bi serves as effective active sites for the enhanced activity toward photocatalytic NRR.

3. Conclusion

In summary, oxygen vacancy-rich Bi/BSO composites were prepared through a one-step hydrothermal process, where BSO nanoparticles were clustering around Bi nanowires and the amount of metallic Bi was manipulated by the initial feed of NaOH. Compared to pure BSO, the Schottky junctions between Bi and BSO in the Bi/BSO composites facilitated the unidirectional electron flow from the semiconducting BSO to the metallic Bi, leading to a significantly enhanced efficiency of photogenerated carrier separation. Concurrently, the formation of Bi nanowires extended the optical absorption of the catalysts to the visible region, leading to a remarkable enhancement of the photocatalytic performance toward ammonia synthesis. The combined experimental and DFT computational analyses showed that the Bi nanowires acted as novel active sites, adsorbing and activating nitrogen molecules via terminal binding, reducing the energy barrier of the protonation process, and accelerating the NRR rate-determining step. Results from this study highlight the fundamental significance of Schottky junctions in the design and engineering of nanocomposite catalysts toward aqueous-phase photocatalytic production of ammonia from nitrogen reduction.

Supporting Information

Supporting Information is available from the Wiley Online Library or from the author.

Acknowledgements

Conflict of Interest

The authors declare no conflict of interest.

Data Availability Statement

The data that support the findings of this study are available from the corresponding author upon reasonable request.

Keywords

[1] L. Zhang, S. Hou, T. Wang, S. Liu, X. Gao, C. Wang, G. Wang, *Small* **2022**, *18*, 2202252.

[2] Z. Yao, S. Liu, H. Liu, Y. Ruan, S. Hong, T.-S. Wu, L. Hao, Y.-L. Soo, P. Xiong, M. M.-J. Li, A. W. Robertson, Q. Xia, L.-X. Ding, Z. Sun, *Adv. Funct. Mater.* **2023**, *33*, 2209843.

[3] J. Yuan, X. Yi, Y. Tang, M. Liu, C. Liu, *Adv. Funct. Mater.* **2020**, *30*, 1906983.

[4] J. Xiong, P. Song, J. Di, H. Li, *Chem. Eng. J.* **2020**, *402*, 126208.

[5] Y. Xia, Y. Xu, X. Yu, K. Chang, H. Gong, X. Fan, X. Meng, X. Huang, T. Wang, J. He, *J. Mater. Chem. A* **2022**, *10*, 17377.

[6] Y. Xiong, B. Li, Y. Gu, T. Yan, Z. Ni, S. Li, J.-L. Zuo, J. Ma, Z. Jin, *Nat. Chem.* **2023**, *15*, 286.

[7] X. Xue, R. Chen, C. Yan, P. Zhao, Y. Hu, W. Zhang, S. Yang, Z. Jin, *Nano Res.* **2019**, *12*, 1229.

[8] C. S. Wang, B. Yan, Z. Z. Chen, B. You, T. Liao, Q. Zhang, Y. Z. Lu, S. H. Jiang, S. J. He, *J. Mater. Chem. A* **2021**, *9*, 25773.

[9] C. Yang, Y. Zhang, F. Yue, R. Du, T. Ma, Y. Bian, R. Li, L. Guo, D. Wang, F. Fu, *Appl. Catal., B* **2023**, *338*, 123057.

[10] Y. Zhang, Q. Wang, S. Yang, H. Wang, D. Rao, T. Chen, G. Wang, J. Lu, J. Zhu, S. Wei, X. Zheng, J. Zeng, *Adv. Funct. Mater.* **2022**, *32*, 2112452.

[11] J. Zander, J. Timm, M. Weiss, R. Marschall, *Adv. Energy Mater.* **2022**, *12*, 2202403.

[12] X. Xue, R. Chen, H. Chen, Y. Hu, Q. Ding, Z. Liu, L. Ma, G. Zhu, W. Zhang, Q. Yu, J. Liu, J. Ma, Z. Jin, *Nano Lett.* **2018**, *18*, 7372.

[13] G. Zhang, Y. Meng, B. Xie, Z. Ni, H. Lu, S. Xia, *Appl Catal B* **2021**, *296*, 120379.

[14] Y. C. Zhang, C. D. Han, J. Gao, L. Pan, J. T. Wu, X. D. Zhu, J. J. Zou, *ACS Catal.* **2021**, *11*, 12485.

[15] G. Wang, T. Huo, Q. Deng, F. Yu, Y. Xia, H. Li, W. Hou, *Appl Catal B* **2022**, *310*, 121319.

[16] X. Xue, H. Chen, R. Xiong, R. Chen, M. Jiang, G. Fu, Z. Xi, X. L. Zhang, J. Ma, W. Fang, Z. Jin, *ACS Appl. Mater. Interfaces* **2021**, *13*, 4975.

[17] H. Xu, Y. Wang, X. Dong, N. Zheng, H. Ma, X. Zhang, *Appl Catal B* **2019**, *257*, 117932.

[18] K.-B. Jiang, W.-Q. Huang, T.-T. Song, P.-X. Wu, W.-F. Wang, Q.-S. Chen, M.-S. Wang, G.-C. Guo, *Adv. Funct. Mater.* **2023**, *33*, 2304351.

[19] X. Xue, R. Chen, C. Yan, Y. Hu, W. Zhang, S. Yang, L. Ma, G. Zhu, Z. Jin, *Nanoscale* **2019**, *11*, 10439.

[20] Y. Huang, Y. Zhu, S. Chen, X. Xie, Z. Wu, N. Zhang, *Adv. Sci.* **2021**, *8*, 2003626.

[21] Y. Sun, Z. Zhao, W. Zhang, C. Gao, Y. Zhang, F. Dong, *J. Colloid Interface Sci.* **2017**, *485*, 1.

[22] S. Zhang, Y. Rong, J. Wei, Z. Li, T. Liang, Z. Yu, H. Zhu, S. Wang, Y. Hou, *J. Colloid Interface Sci.* **2023**, *629*, 604.

[23] D. J. Zhou, P. S. Li, X. Lin, A. McKinley, Y. Kuang, W. Liu, W. F. Lin, X. M. Sun, X. Duan, *Chem. Soc. Rev.* **2021**, *50*, 8790.

[24] M. Kim, H. Ju, J. Kim, *Chem. Eng. J.* **2019**, *358*, 11.

[25] J. Xiong, J. Di, J. Xia, W. Zhu, H. Li, *Adv. Funct. Mater.* **2018**, *28*, 1801983.

[26] J. Di, J. Xia, M. F. Chisholm, J. Zhong, C. Chen, X. Cao, F. Dong, Z. Chi, H. Chen, Y.-X. Weng, J. Xiong, S.-Z. Yang, H. Li, Z. Liu, S. Dai, *Adv. Mater.* **2019**, *31*, 1807576.

[27] Y. Zhang, J. Di, X. Qian, M. Ji, Z. Tian, L. Ye, J. Zhao, S. Yin, H. Li, J. Xia, *Appl Catal B* **2021**, *299*, 120680.

[28] N. N. Rao, S. Dube, Manjubala, P. N., *Appl Catal B* **1994**, *5*, 33.

[29] K. T. Ranjit, T. K. Varadarajan, B. Viswanathan, *J Photochem Photobiol A Chem* **1996**, *96*, 181.

[30] J. Greeley, T. F. Jaramillo, J. Bonde, I. Chorkendorff, J. K. Nørskov, *Nat. Mater.* **2006**, *5*, 909.

[31] A. Kumar, V. Krishnan, *Adv. Funct. Mater.* **2021**, *31*, 2009807.

[32] Y. Guo, Y. Hu, X. Luo, S. Lin, J. Hu, Y. Liu, *Inorg. Chem. Commun.* **2021**, *128*, 108558.

[33] W. Dong, Y. Sun, W. Hua, Y. Yao, G. Zhuang, X. Lv, Q. Ma, D. Zhao, *Adv. Funct. Mater.* **2016**, *26*, 964.

[34] Y. Zhao, L. Zheng, R. Shi, S. Zhang, X. Bian, F. Wu, X. Cao, G. I. N. Waterhouse, T. Zhang, *Adv. Energy Mater.* **2020**, *10*, 2002199.

[35] H. Z. Zhou, F. M. Jin, B. Wu, J. L. Cao, X. K. Duan, A. Kishita, *J. Phys.: Conf. Ser.* **2010**, *215*, 012125.

[36] X. a. Dong, Z. Cui, X. Shi, P. Yan, Z. Wang, A. C. Co, F. Dong, *Angew. Chem., Int. Ed.* **2022**, *61*, e202200937.

[37] G. Dong, X. Huang, Y. Bi, *Angew. Chem., Int. Ed.* **2022**, *61*, e202204271.

[38] Y. Lu, M. Chen, T. Huang, Y. Huang, J.-J. Cao, H. Li, W. Ho, S. C. Lee, *Environ Sci: Nano* **2021**, *8*, 1927.

[39] Y. Zhao, R. Shi, X. Bian, C. Zhou, Y. Zhao, S. Zhang, F. Wu, G. I. N. Waterhouse, L.-Z. Wu, C.-H. Tung, T. Zhang, *Adv. Sci.* **2019**, *6*, 1802109.

[40] Y. Yu, C. Cao, H. Liu, P. Li, F. Wei, Y. Jiang, W. Song, *J. Mater. Chem. A* **2014**, *2*, 1677.

[41] Z. Wang, C. Jiang, R. Huang, H. Peng, X. Tang, *J. Phys. Chem. C* **2014**, *118*, 1155.

[42] J. Toudert, R. Serna, M. Jiménez de Castro, *J. Phys. Chem. C* **2012**, *116*, 20530.

[43] H. Yuan, L. Wang, L. Xu, Q. Han, H. Jia, X. Sun, *Ceram. Int.* **2022**, *48*, 2710.

[44] J. Ran, T. Y. Ma, G. Gao, X.-W. Du, S. Z. Qiao, *Energy Environ. Sci.* **2015**, *8*, 3708.

[45] Y. Cao, L. Guo, M. Dan, D. E. Doronkin, C. Han, Z. Rao, Y. Liu, J. Meng, Z. Huang, K. Zheng, P. Chen, F. Dong, Y. Zhou, *Nat. Commun.* **2021**, *12*, 1675.

[46] Y. Kojima, M. Yamaguchi, *Int. J. Hydrogen Energy* **2021**, *46*, 2306.

[47] Y. J. Choi, S. Kim, S. H. J. Woo, Y. J. Song, E. Hwang, M. S. Kang, J. H. Cho, *ACS Nano* **2020**, *14*, 16036.

[48] S. Gao, R. Wu, M. Sun, M. Guo, D. B. DuBois, S. Chen, H. Ji, C. Wang, Q. Wang, *Appl. Catal., B* **2023**, *324*, 122260.

[49] S. Gao, H. Ji, P. Yang, M. Guo, J. Tressel, S. Chen, Q. Wang, *Small* **2023**, *19*, 2206114.

[50] J. Di, C. Chen, Y. Wu, Y. Zhao, C. Zhu, Y. Zhang, C. Wang, H. Chen, J. Xiong, M. Xu, J. Xia, J. Zhou, Y. Weng, L. Song, S. Li, W. Jiang, Z. Liu, *Adv. Mater.* **2022**, *34*, 2204959.

[51] H. Li, J. Shang, Z. Ai, L. Zhang, *J. Am. Chem. Soc.* **2015**, *137*, 6393.

[52] S. Wang, X. Hai, X. Ding, K. Chang, Y. Xiang, X. Meng, Z. Yang, H. Chen, J. Ye, *Adv. Mater.* **2017**, *29*, 1701774.

[53] Y. Fan, F. Wang, R. Li, C. Liu, Q. Fu, *ACS Catal.* **2023**, *13*, 2277.

[54] X.-Y. Xie, P. Xiao, W.-H. Fang, G. Cui, W. Thiel, *ACS Catal.* **2019**, *9*, 9178.

[55] J. Yuan, W. Feng, Y. Zhang, J. Xiao, X. Zhang, Y. Wu, W. Ni, H. Huang, W. Dai, *Adv. Mater.* **2023**, *36*, 2303845.

[56] J.-C. Liu, X.-L. Ma, Y. Li, Y.-G. Wang, H. Xiao, J. Li, *Nat. Commun.* **2018**, *9*, 1610.